

This is a preprint of the following article, which is available at: <http://mdolab.engin.umich.edu>  
Jichao Li, Sicheng He, and Joaquim R. R. A. Martins. Data-driven constraint approach to ensure low-speed performance in transonic aerodynamic shape optimization. *Aerospace Science and Technology*, 92 (2019) 536-550. doi:10.1016/j.ast.2019.06.008.

The original article may differ from this preprint and is available at:  
<https://doi.org/10.1016/j.ast.2019.06.008>.

# Data-driven Constraint Approach to Ensure Low-speed Performance in Transonic Aerodynamic Shape Optimization

Jichao Li, Sicheng He, and Joaquim R. R. A. Martins

*Department of Aerospace Engineering, University of Michigan, Ann Arbor, MI, 48109*

## Abstract

Aerodynamic shape optimization based on computational fluid dynamics has the potential to become more widely used in the industry; however, the optimized shapes are often criticized for not being practical. Techniques seeking more practical results, such as multipoint optimization and geometric constraints, are either ineffective or too time consuming because they require trial and error. We propose a data-driven constraint for the aerodynamic shape optimization of aircraft wings that ensures the overall practicality of the optimum shape, with a focus on achieving a good low-speed performance. The constraint is formulated by extracting the relevant features from an airfoil database via modal analysis, correlation analysis, and Gaussian mixture models. The optimization results demonstrated that this approach addresses the thin leading edge issue that had plagued previous optimization results, and further analysis demonstrated that this data-driven constraint ensures good low-speed off-design performance without sacrificing the transonic on-design performance. The proposed approach can use other airfoil databases and can even be generalized to other shape optimization and engineering design problems.

## 1 Introduction

Aircraft aerodynamic efficiency directly affects operating costs and greenhouse gas emissions. Aerodynamic shape optimization based on computational fluid dynamics (CFD) has been applied to airfoil and wing design to improve the cruise efficiency [1–9]. However, aerodynamic shape optimization tends to overstate its benefits because it improves the on-design performance to the detriment of the off-design performance [4, 10, 11]. Special care is required in aerodynamic shape optimization to prevent the

design from converging to unrealistic shapes [12]. For example, some of the previous efforts have produced thin leading edges, which deteriorate the off-design performance, especially at low speeds [10].

Multipoint optimization can address this issue to a certain extent. Lyu et al. [10] showed that multipoint optimization can alleviate the thin leading edge issue in the optimization of the Common Research Model (CRM) wing. To eliminate the heuristics involved in choosing the flight conditions and corresponding weights, Liem et al. [7] proposed an approach to formulate the multipoint drag function based on cruise flight data. However, multipoint optimization in the transonic regime is designed to improve the robustness with respect to flight conditions around the cruise nominal condition; therefore, it does not directly address the thin leading edge issue, which mainly affects the low-speed performance of the clean wing. Nemec et al. [11] studied multipoint airfoil design optimization in the transonic flow regime, but this issue was not addressed. Kenway and Martins [13] studied the effect of different weights of cruise conditions on the multipoint optimization of the CRM wing; however, the thin leading edge issue persisted. To achieve a more practical airfoil design, Buckley et al. [4] enforced a maximum lift coefficient ( $C_{L,\max}$ ) constraint in a multipoint optimization and they obtained a more reasonable shape. However, the evaluation of  $C_{L,\max}$  for a given design using CFD requires higher fidelity than what the Reynolds-averaged Navier–Stokes equations (RANS) can provide and is still an open problem. Constraining buffet can also help address off-design performance [14].

Another technique that can be used to achieve more realistic airfoil shapes is to add explicit geometric constraints, such as radius or thickness constraints at the leading edge [14–16]. While this technique does help, the optimized design is sensitive to the form and value of these constraints. Therefore, these constraints require trial and error and experience to evaluate the suitability of the final results.

To bypass the trial-and-error process, we propose using the design experience implicitly embedded in existing airfoil designs. Our hypothesis is that we can construct a numerical constraint based on the analysis of an existing airfoil database. We used a publicly available airfoil database that contains more than 1500 airfoils for different applications.<sup>1</sup> Most of these airfoils are designed by considering various requirements, including the low-speed performance and structural demands, and many of them have been validated through wind-tunnel experiments and actual flight.

The proposed data-driven approach provides a systematic method for deriving a differentiable function to represent an optimization constraint and involves multiple steps. First, we compute the dominant thickness and camber modes from the airfoil geometries in the database and analyze the correlations between these modes. We compare the distributions in these correlations with previously optimized airfoils that exhibit leading edges that are unrealistically thin to find the most relevant characteristics that define realistic airfoil shapes. Then, we use Gaussian mixture models (GMMs) and their associated probabilities to quantify the extent to which a given airfoil or a wing section exhibits the relevant characteristics. The probability function is differentiable and suitable for gradient-based optimization.

---

<sup>1</sup><http://webfoil.engin.umich.edu>

We use this data-driven function to constrain the airfoil and wing section shapes in CFD-based aerodynamic shape optimization, and we investigate the effect of adding this constraint to different sections in wing design optimization. Further analyses of the optimized results demonstrate that this data-driven approach addresses the thin leading edge issue and improves the low-speed performance without significantly decreasing the benefit to the transonic regime.

The rest of this paper is organized as follows. First, in Section 2, we discuss how to preprocess existing airfoil data in the database, capture the distribution features among the thickness and camber modes, and formulate the data-driven constraint function. Then, in Section 3, we formulate the constraint with the data-driven function in the airfoil design optimization. In Section 4, we extend this approach to three dimensions in the optimization of the CRM wing. Finally, in Section 5, we end this paper with a summary of conclusions.

## 2 Data-Driven Constraint Formulation

### 2.1 Airfoil Data Processing

Features embedded in proven airfoils can be of great value to aerodynamic design. We used a publicly available airfoil database to conduct feature analyses. These airfoils are designed for a wide range of applications, from low-Reynolds-number airfoils for unmanned aerial vehicles and model aircraft to jet transports and wind turbines. However, the airfoil data are not provided in a uniform format, and, therefore, we developed a process to clean the data and make them consistent.

We used the procedure illustrated in Figure 1 to process the data in three main steps: formatting, normalization, and selection. Most of the airfoils are provided in an  $(x, y)$  format starting from the trailing edge, following the upper surface to the leading edge, and back to the trailing edge along the lower surface. However, there are some exceptions to this format. Some airfoils do not form a closed loop (including airfoils with a finite trailing edge thickness), some coordinates are provided for a nonzero angle of attack, and several airfoils exhibit large oscillations in shape.

We modified all the airfoils to have a sharp trailing edge. After eliminating incomplete airfoils, we were left with 1458 airfoils. Similar to our previous work with this airfoil database [17], we applied a smoothing procedure to all airfoil coordinates to reduce the small oscillations in the shapes. This procedure is implemented in Python and is available under an open-source license <sup>2</sup>.

### 2.2 Correlation Analysis of the Thickness and Camber Modes

There are different characteristics that can be used to measure airfoils, such as the camber, thickness, and leading edge radius. Here, we characterize airfoil shapes using modes computed via singular value decomposition, as done in previous efforts [18–20]. We separate the modes for the camber and thickness lines because they are more intuitive and they inherently represent different information [18]. Camber distribution

---

<sup>2</sup>[https://github.com/npuljc/Airfoil\\_preprocessing](https://github.com/npuljc/Airfoil_preprocessing)

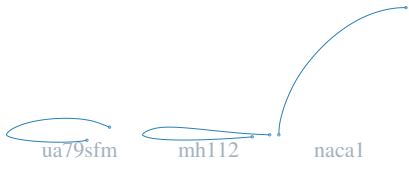















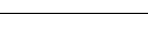

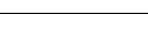

















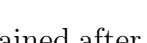
Procedure	Step	Eliminated airfoils	Selected airfoils
Step 1 Formatting	1.1 Delete texts in airfoil data files.	3	1547
	1.2 Ensure coordinates are in this sequence: trailing edge-upper surface-leading edge-lower surface-trailing edge.		
	1.3 Eliminate incomplete airfoils.		
Step 2 Normalization	2.1 Sharpen trailing edge if blunt.	48	1498
	2.2 Define leading edge by finding the farthest point on curve.	  	
	2.3 Normalize coordinates by making the chord equal to one and angle of attack zero.	  	
		  	
		  	
Step 3 Selection	2.4 Save airfoil in uniform format.	  	1458
		  	
	3.1 Remove airfoils with more than one maximum thickness location.	40	
		  	
		  	
		  	1458
		  	
		  	
		  	

Figure 1: A total of 1458 consistent airfoil geometries were obtained after preprocessing the airfoil database.

has a large impact on lift and pitching moments, while thickness distribution primarily affects drag and directly relates to structural requirements. We obtain the modes via singular value decomposition. Suppose we put all airfoil coordinates into a matrix  $\mathbf{A}$ , where each column corresponds to an airfoil. The singular value decomposition of this matrix can be expressed as

$$\mathbf{A} = \mathbf{U}\mathbf{\Sigma}\mathbf{V}^\top, \quad (1)$$

where each column of  $\mathbf{U}$  corresponds to a mode shape and  $\mathbf{\Sigma}$  is a diagonal matrix with the singular values. To obtain airfoil shapes based on these modes, we select the modes corresponding to the largest singular values to obtain a matrix of the dominant modes,



$\Phi$ . Then, the  $y$ -coordinate values can be expressed by

$$\mathbf{y}_{\text{airfoil}} = \Phi \mathbf{c}_{\text{mode}}, \quad (2)$$

where  $\mathbf{c}_{\text{mode}}$  is a vector of coefficients corresponding to each mode.

The first five camber and thickness modes derived from the airfoil database and their effect on some airfoil shapes are shown in Figure 2. For example, the first thickness mode increases or decreases the whole airfoil thickness, while the second one decreases the thickness of the rear while increasing it in the front.

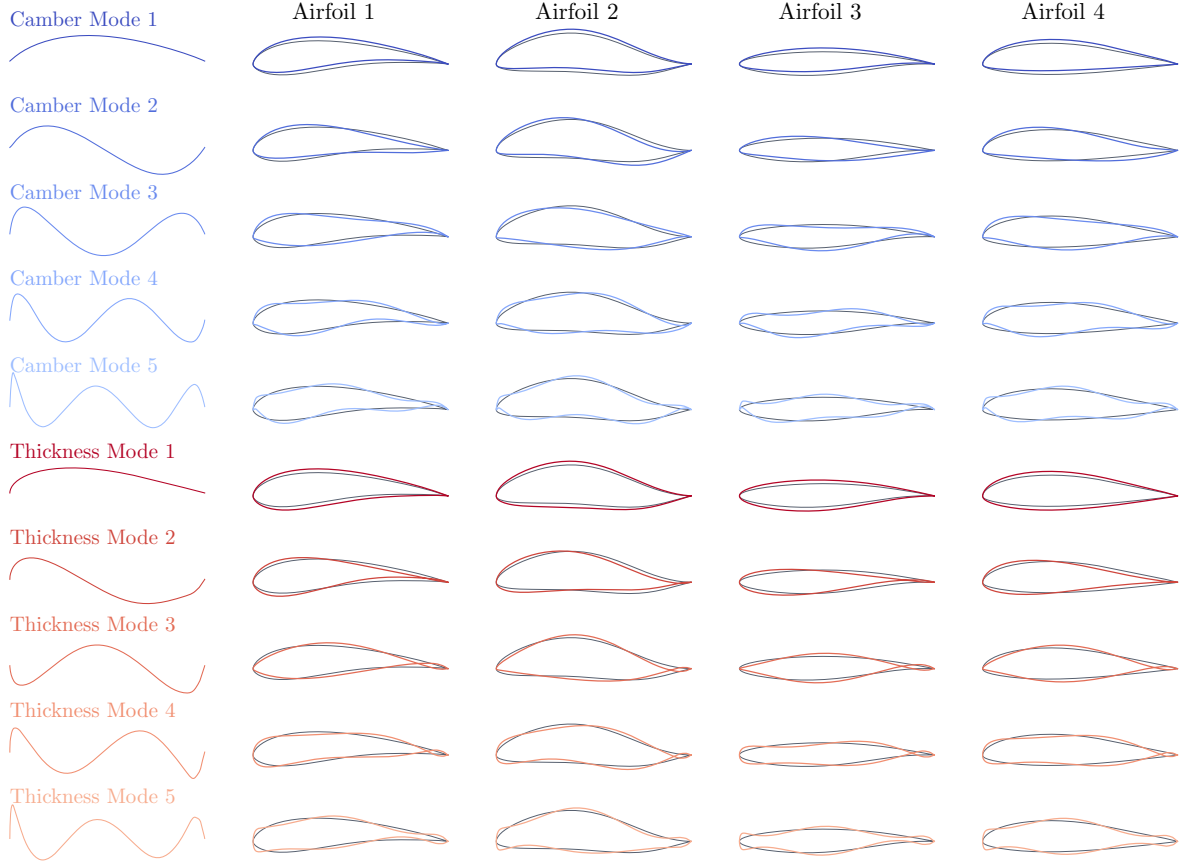


Figure 2: Effect of camber and thickness modes on airfoil testing.

The correlation between the  $i$ th and the  $j$ th mode coefficient is defined as

$$\rho_{c_i, c_j} = \frac{\sum_{l=1}^N (c_i^{(l)} - \bar{c}_i)(c_j^{(l)} - \bar{c}_j)}{\sqrt{\sum_{l=1}^N (c_i^{(l)} - \bar{c}_i)^2 \sum_{l=1}^N (c_j^{(l)} - \bar{c}_j)^2}}, \quad (3)$$

where the average mode coefficients are

$$\bar{c}_i = \frac{1}{N} \sum_{l=1}^N c_i^{(l)}, \quad \bar{c}_j = \frac{1}{N} \sum_{l=1}^N c_j^{(l)}. \quad (4)$$

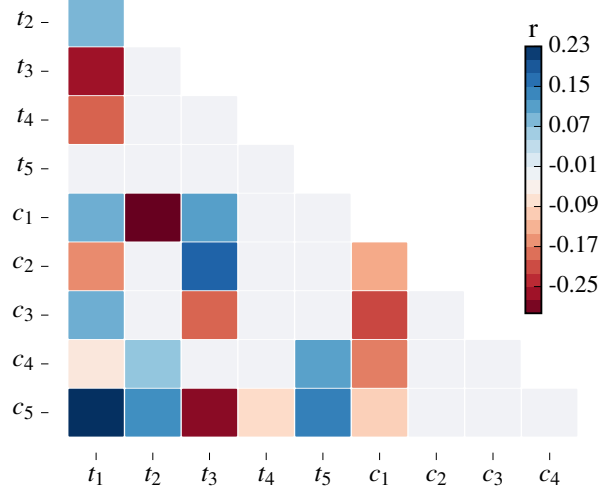


Figure 3: Correlation between the camber and the thickness mode coefficients derived from the airfoil database.

Figure 3 shows the correlation between the camber and thickness mode coefficients, where the color map represents the correlation coefficient  $\rho_{c_i, c_j}$ .

Figure 4 shows the distributions of all airfoils (blue dots) in the space of related pairs between the five camber and thickness modes. We also show the airfoils obtained from previous aerodynamic shape optimizations [10, 13] that we consider unrealistic (red ‘x’).



Figure 4: Distribution of airfoils and some unrealistic airfoils in the planes of related modes.

Most of the related modes approximately obey the Gaussian distributions, which do not convey useful features, and the unrealistic airfoils are almost within the airfoil database in these distributions. However, the distribution between the first and the third thickness mode is not a typical Gaussian one, and the unrealistic airfoils are clearly outside the distribution domain of all airfoils. The first thickness mode increases the thickness at the leading edge, while the third one decreases it. The coefficients of the third thickness mode for the unrealistic airfoils are unusually large because they have such thin leading edges. Given the trends observed in this distribution, we can now quantify the desired characteristics from this correlation and constrain these characteristics in an optimization.

## 2.3 Data-Driven Constraint

We quantify the desirable characteristics for the airfoils using a GMM, which is a mixture of a finite number of Gaussian distributions. The GMM represents normally distributed subpopulations of an overall population without requiring knowledge about which subpopulation a data point belongs to. This is a form of unsupervised learning that allows the model to learn the subpopulations automatically. The probability density function  $p(\mathbf{x})$  of the GMM is represented as a weighted sum of Gaussian component densities [21]:

$$p(\mathbf{x}) = \sum_{i=1}^K \phi_i \mathcal{N}(\mathbf{x} | \boldsymbol{\mu}_i, \boldsymbol{\Sigma}_i), \quad (5)$$

where  $\mathbf{x}$  is the  $D$ -dimensional input;  $\phi_i$  (where  $i = 1, \dots, K$ ) are the combination weights, which add up to 1 ( $\sum_{i=1}^K \phi_i = 1$ ); and  $K$  is the number of Gaussian components. The  $i^{\text{th}}$  Gaussian density is

$$\mathcal{N}(\mathbf{x} | \boldsymbol{\mu}_i, \boldsymbol{\Sigma}_i) = \frac{1}{\sqrt{(2\pi)^D |\boldsymbol{\Sigma}_i|}} \exp\left(-\frac{1}{2}(\mathbf{x} - \boldsymbol{\mu}_i)^\top \boldsymbol{\Sigma}_i^{-1}(\mathbf{x} - \boldsymbol{\mu}_i)\right) \quad (6)$$

where  $\boldsymbol{\mu}_i$  and  $\boldsymbol{\Sigma}_i$  are the mean vector and the covariance matrix of this component density, respectively. An example of a GMM is shown in Figure 5, where three functions (on the left) get mixed into a single smooth function (on the right).

The difficulty in the construction of a GMM lies in determining which points came from which latent component, and then it is easy to fit a separate Gaussian distribution to each set of points. To determine this, we use the iterative expectation-maximization (EM) algorithm [22] to compute the model parameters. The basic idea of the EM algorithm is to iteratively maximize the likelihood function  $p(\mathbf{X})$ .  $\mathbf{X}$  is the training data set  $\mathbf{x}_1, \dots, \mathbf{x}_N$  and

$$p(\mathbf{X}) = \prod_{n=1}^N p(\mathbf{x}_n), \quad (7)$$

where the means  $\boldsymbol{\mu}_i$ , covariances  $\boldsymbol{\Sigma}_i$ , and mixing coefficients  $\phi_i$  are initialized with the  $k$ -means algorithm [23], which is an unsupervised clustering method with a low computational cost. Then, we apply the EM algorithm to update the parameters iteratively.

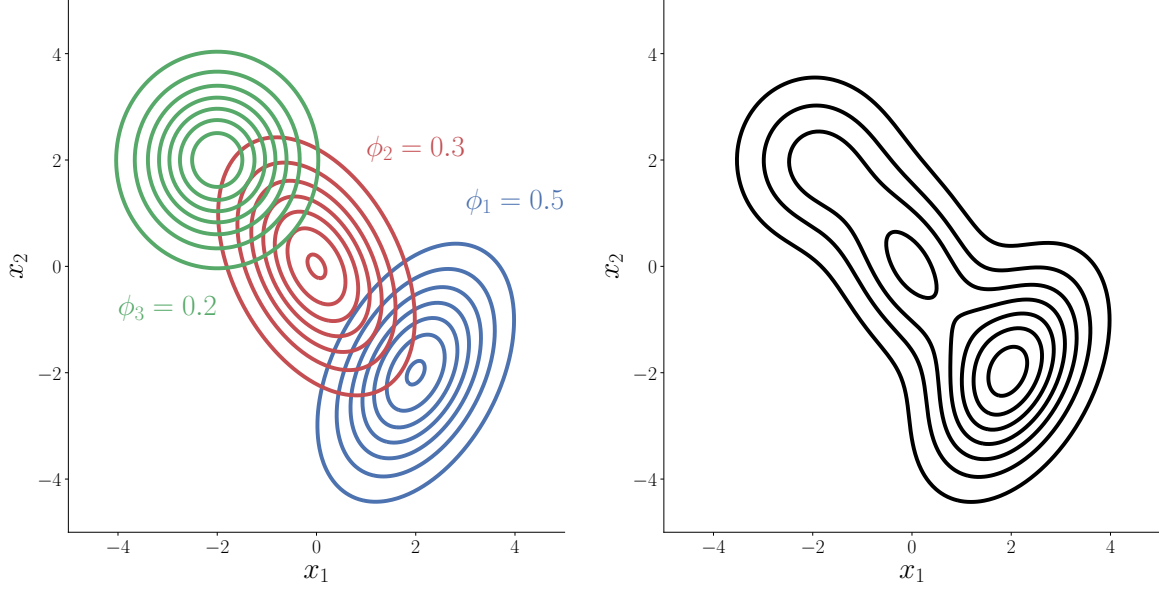


Figure 5: A GMM with three components. Three individual Gaussian components with different weights (left) become a single smooth function using the GMM (right). The distribution is biased toward the function with the largest weight.

In the “ $E$ ” step, we calculate the responsibilities using the current parameters:

$$\Pr(k|\mathbf{x}_n) = \frac{\phi_k \mathcal{N}(\mathbf{x}_n | \boldsymbol{\mu}_k, \boldsymbol{\Sigma}_k)}{\sum_{i=1}^K \phi_i \mathcal{N}(\mathbf{x}_n | \boldsymbol{\mu}_i, \boldsymbol{\Sigma}_i)}. \quad (8)$$

Then, in the “ $M$ ” step, the parameters are re-estimated with the following formulas:

$$\begin{aligned} \hat{\phi}_i &= \frac{1}{N} \sum_{n=1}^N \Pr(i|\mathbf{x}_n) \\ \hat{\boldsymbol{\mu}}_i &= \frac{\sum_{n=1}^N \Pr(i|\mathbf{x}_n) \mathbf{x}_n}{\sum_{n=1}^N \Pr(i|\mathbf{x}_n)} \\ \hat{\boldsymbol{\Sigma}}_i &= \frac{\sum_{n=1}^N \Pr(i|\mathbf{x}_n) \mathbf{x}_n \mathbf{x}_n^\top}{\sum_{n=1}^N \Pr(i|\mathbf{x}_n)} - \hat{\boldsymbol{\mu}}_i \hat{\boldsymbol{\mu}}_i^\top, \end{aligned} \quad (9)$$

where “ $\hat{\cdot}$ ” represents an updated parameter.

Because the GMM is completely determined by the parameters of its individual components, a fitted GMM can give an estimate of the probabilities of both in-sample and out-of-sample data points, which is known as density estimation. We use the GMM to capture the distribution feature between the first and the third thickness mode, and use its probability density function to detect the abnormality. We investigated the effect from the number of components in the GMM and found that the likelihood function does not increase after the fifth component is added. Therefore, we use five components to construct the GMM. Figure 6 shows the log-probability density function

$f_{\text{GMM}}(\mathbf{x})$ , where

$$f_{\text{GMM}}(\mathbf{c}_{\text{mode}}) = \log_{10} p((c_1, c_3)), \quad (10)$$

and  $c_1$  and  $c_3$  are the first and third coefficients, respectively, for the thickness modes in  $\mathbf{c}_{\text{mode}}$ . The previously obtained unrealistic airfoils (red ones) are in the domain corresponding to  $f_{\text{GMM}} \leq -1.2$ . The airfoils (black ones) in the original CRM wing sections are in the domain with  $f_{\text{GMM}} \geq 1.6$ , which is well within the desired range.

Figure 7 shows airfoil distribution probabilities with respect to  $f_{\text{GMM}}$ . Most airfoils are in the domain corresponding to positive  $f_{\text{GMM}}$  values, and airfoils with significantly negative values are not typical transonic ones. Defining outlier shapes using  $f_{\text{GMM}} \geq -1.0$ ,  $f_{\text{GMM}} \geq 0.0$ , and  $f_{\text{GMM}} \geq 0.6$  results in domains including 95.1%, 90.7%, and 85.0% of the airfoils, respectively.

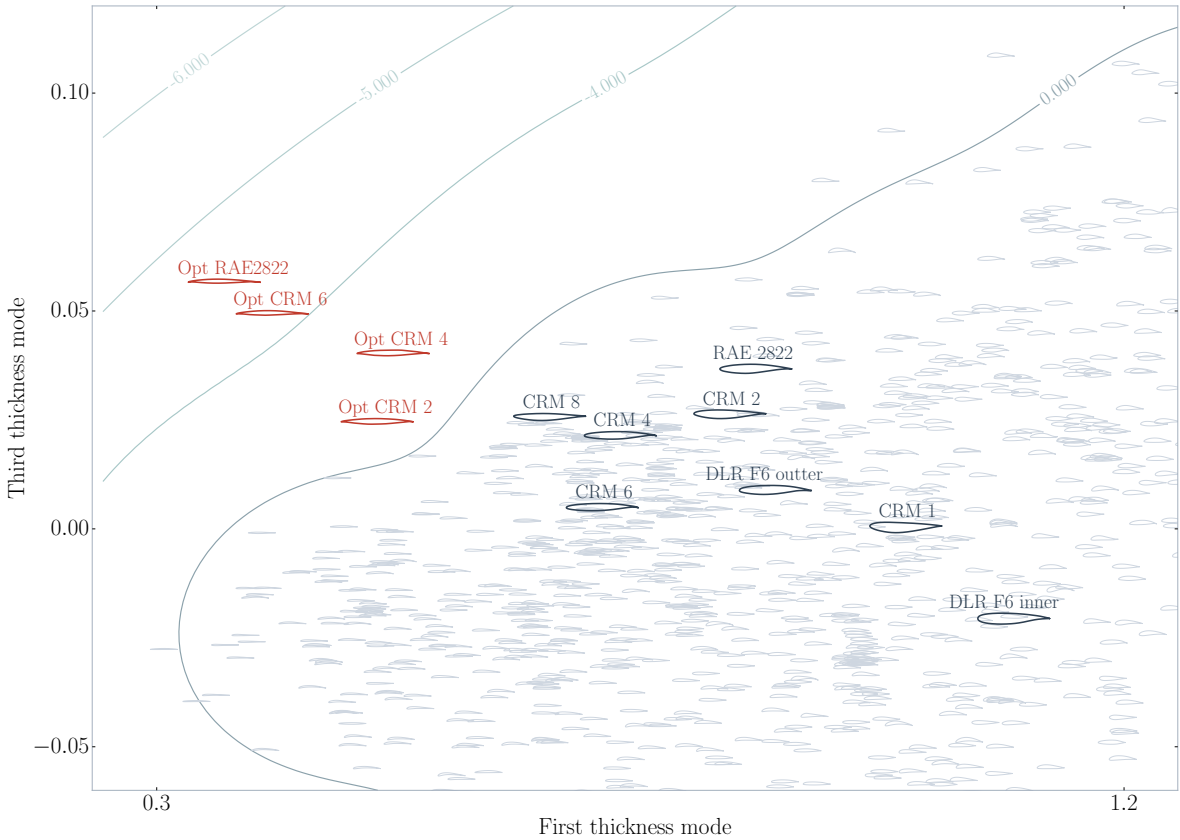


Figure 6: Log-probability density function of the GMM between the first and the third thickness mode

To reduce the aerodynamic drag, the optimization algorithm tends to decrease the thickness by reducing the first thickness mode magnitude, which dominates the overall thickness. However, if the third thickness mode magnitude is not reduced simultaneously, unrealistic airfoils with thin leading edges and significantly negative  $f_{\text{GMM}}$  values would be involved, including the previously optimized airfoils shown in Figure 6 (highlighted in red). Thus, constraining the function  $f_{\text{GMM}}$  in an aerodynamic shape optimization should ensure realistic airfoils.

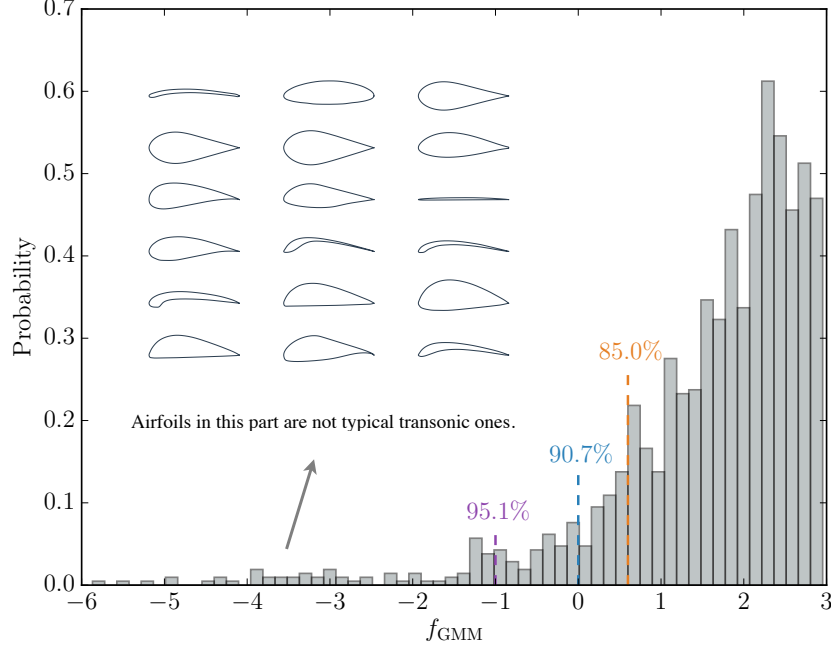


Figure 7: Histogram of the airfoil distribution with respect to  $f_{\text{GMM}}$ .

This constraint plays a similar role to explicit geometric constraints on the leading edge thickness or radius, although it is more robust as it improves the low-speed performance with a much lesser negative effect on the transonic regime. We demonstrate this robustness in aerodynamic optimization by using different  $f_{\text{GMM}}$  lower bounds in Section 3.

## 3 Airfoil Design Optimization

### 3.1 Problem Description

To evaluate the proposed approach, we implemented it in a CFD-based aerodynamic shape optimization framework and applied it to solve a benchmark airfoil optimization case.

The CFD solver was ADflow [24–27], which is available under an open-source license.<sup>3</sup> ADflow solves the RANS using a second-order finite-volume scheme. It can handle structured multiblock and overset meshes using the Spalart–Allmaras (SA) turbulence model. The shape parametrization that defines the design variables was performed using free-form deformation (FFD) [28]. The optimizer we used was the Sparse Nonlinear OPTimizer (SNOPT) [29], which is a gradient-based quasi-Newton optimizer suitable for optimization problems featuring many sparse nonlinear constraints [30]. We used SNOPT through the pyOptSparse Python interface [31]<sup>4</sup>.

ADflow includes a discrete adjoint solver [25, 32] that efficiently computes the sensitivities of force coefficients with respect to large numbers of design variables. To add

<sup>3</sup><https://github.com/mdolab/adflow>

<sup>4</sup><https://github.com/mdolab/pyoptsparse>

the data-driven constraint  $f_{\text{GMM}}$  to the gradient-based optimization, we evaluated its gradient with respect to the shape design variables  $\mathbf{y}_{\text{shape}}$ , which is computed using the chain rule

$$\frac{df_{\text{GMM}}}{d\mathbf{y}_{\text{shape}}} = \frac{df_{\text{GMM}}}{d\mathbf{c}_{\text{mode}}} \frac{d\mathbf{c}_{\text{mode}}}{d\mathbf{y}_{\text{airfoil}}} \frac{d\mathbf{y}_{\text{airfoil}}}{d\mathbf{y}_{\text{shape}}}, \quad (11)$$

where  $\mathbf{y}_{\text{airfoil}}$  are the airfoil or wing section coordinates. We computed  $df_{\text{GMM}}/d\mathbf{y}_{\text{mode}}$  and  $d\mathbf{c}_{\text{mode}}/d\mathbf{y}_{\text{airfoil}}$  using Eqs. (10) and (2), respectively. We evaluated  $d\mathbf{y}_{\text{airfoil}}/d\mathbf{y}_{\text{shape}}$  using the FFD parametrization implemented by Kenway et al. [28].

The airfoil optimization problem we solved was the Aerodynamic Design Optimization Discussion Group (ADODG) Case 2 benchmark, which defines the drag minimization problem detailed in Table 1 starting from an RAE 2822 airfoil. This problem has been solved by various researchers [33–35].

Table 1: Optimization problem statement in the airfoil design

	Function	Description	Quantity
Minimize	$C_d$	Drag coefficient	1
With respect to	$\mathbf{y}_{\text{shape}}$	$y$ perturbations of the FFD control points	40
	$\alpha$	Angle of attack	1
Subject to	$\Delta y_{\text{LE,upper}} =$ $-\Delta y_{\text{LE,lower}}$	Fixed leading edge constraint	1
	$\Delta y_{\text{TE,upper}} =$ $-\Delta y_{\text{TE,lower}}$	Fixed trailing edge constraint	1
	$C_l = 0.824$	Lift constraint	1
	$C_m \geq -0.092$	Pitching moment constraint	1
	$A \geq k_{\text{area}} A_{\text{init}}$	Area constraint	1

A  $20 \times 2$  FFD control box was used to parameterize the airfoil shape, as shown in Figure 8. We verified the accuracy of the data-driven constraint gradient (11) via the finite-difference method with the marked control points in Figure 8. The normalized error was computed as  $\varepsilon = |g' - g'_{\text{FD}}|/|g'|$ , where  $g'$  and  $g'_{\text{FD}}$  are the gradient values given by Eq. (11) and finite differences, respectively. Owing to truncation cancellation errors, the finite-difference gradient was only accurate with a suitable difference step size, which can be found by a step-size study [36]. Using the appropriate step sizes, we found the normalized errors to be around  $10^{-8}$ , as shown in Figure 9.

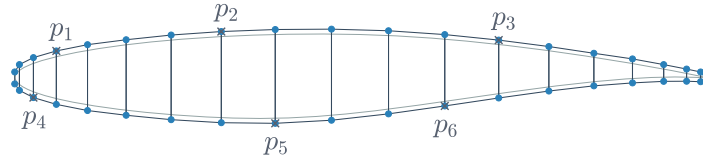


Figure 8: FFD box used in the airfoil optimization, showing the design variables used in the gradient verification.



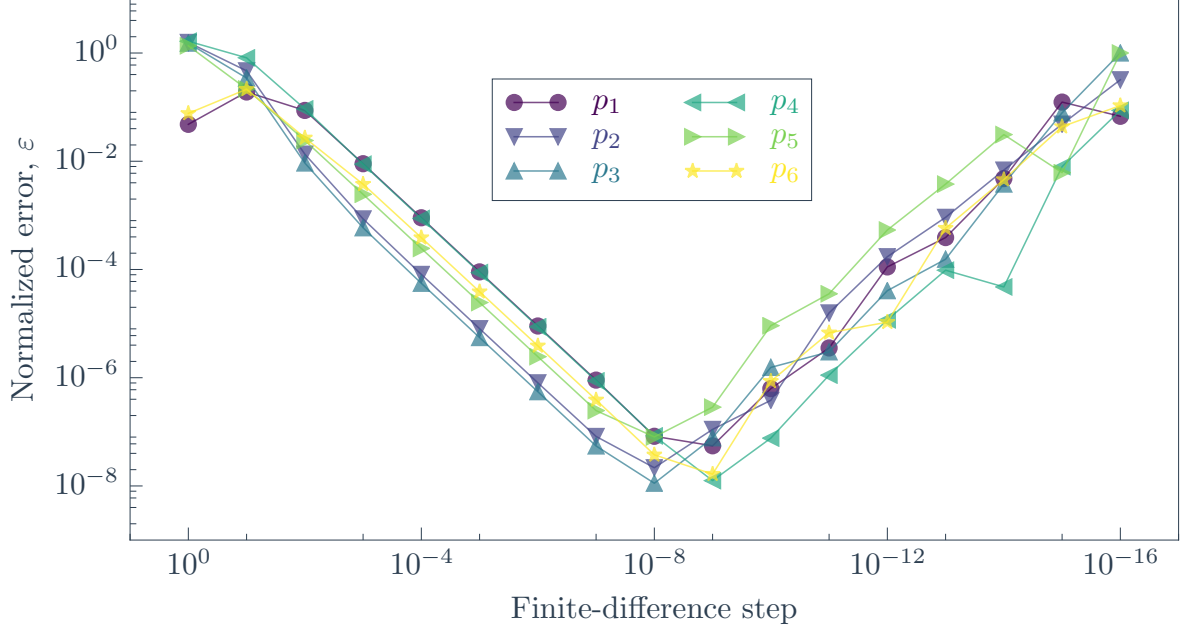


Figure 9: The gradient given by Eq. (11) agrees well with the finite-difference gradient when using a step size of around  $10^{-8}$ .

As shown in Table 1, there is one geometric constraint in the ADODG case, which prevents the cross-sectional area from decreasing by more than a factor of  $k_{\text{area}}$ . This constraint prevents the optimization from converging to unrealistic shapes to some extent. However, the value of this area has a large effect on the optimum shape. To study the effect of the area constraint value, we solved this problem with five different values of  $k_{\text{area}}$ . In addition to the constraints shown in Table 1, we added 30 thickness constraints along the chord to prevent the upper and lower surfaces from crossing.

### 3.2 Optimization With Different Constraints

The optimization results with different area constraints are shown in Figure 10. All the optimizations converge to airfoils with shock-free pressure distributions, and, therefore, their drag coefficients are all reduced. However, the leading edge of the optimized airfoils becomes sharper as the area constraint decreases. This would be an issue for structural design and has a negative impact on the low-speed aerodynamic performance of the clean wing as well.

To address this issue, we could explicitly add a constraint on the thickness or radius of the leading edge to prevent it from decreasing during the optimization. As previously discussed, this approach requires trial and error for each specific case. The data-driven constraint proposed herein can be regarded as an implicit geometric constraint. We compared the performance of both approaches in the airfoil optimization with  $k_{\text{area}} = 0.4$ . The explicit geometric constraint was set to  $x/c = 0.002$  to prevent the thickness from decreasing. To show the robustness of the data-driven constraint approach, we used three lower bounds, i.e.,  $f_{\text{GMM}} \geq -1.0$ ,  $f_{\text{GMM}} \geq 0.0$ , and  $f_{\text{GMM}} \geq 0.6$ , according to the analysis in Figure 7. In the following context, we note these two types

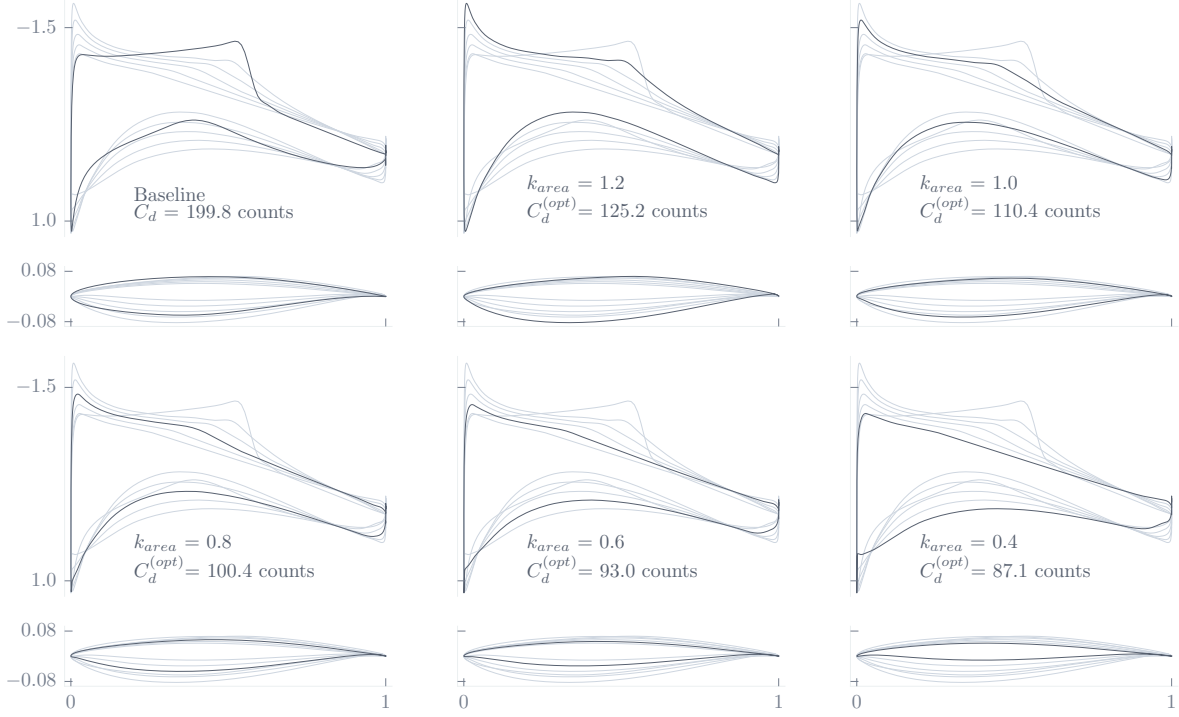


Figure 10: Optimization with different area constraints. As the allowable area decreases, the airfoil leading edge becomes much sharper.

of constraints as the *thickness constraint* and the *data-driven constraint*, respectively, and the optimization with the basic area constraint (Figure 10) is noted as the *basic constraint*.

Similar to the results in Figure 10, the optimization with both the thickness and the data-driven constraints converges to shock-free shapes, as shown in Figure 11. These results do not exhibit the type of unrealistic thin leading edges obtained using only the basic constraint. However, the thickness constraint results in an unrealistic shape for the trailing edge, while the shapes obtained with the proposed data-driven constraint look more realistic. Thus, data-driven constraints achieve slightly smaller drag coefficients than those of the thickness constraint. Furthermore, the three  $f_{\text{GMM}}$  lower bounds lead to similar optimized shapes and  $C_p$  distributions, which demonstrate the robustness of the data-driven constraint.

We also performed an eleven-point optimization as a comparison, where the objective function was the weighted average  $C_d$  of all design points. Other than the cruise design point with  $M = 0.734$  and  $C_l = 0.824$  in ADODG Case 2, 10 other design points in both subsonic and transonic regimes were involved, as shown in Figure 12. For a multipoint design optimization to be credible, the flight conditions and respective weights have to be appropriate [7]. We chose the weights according to the analyses of previous optimization results and emphasize the transonic conditions to ensure a cruise performance. This multipoint optimization yields an optimum with a leading edge thicker than that of the single-point optimum with the basic constraint, and it is close to optima obtained with the data-driven constraints.

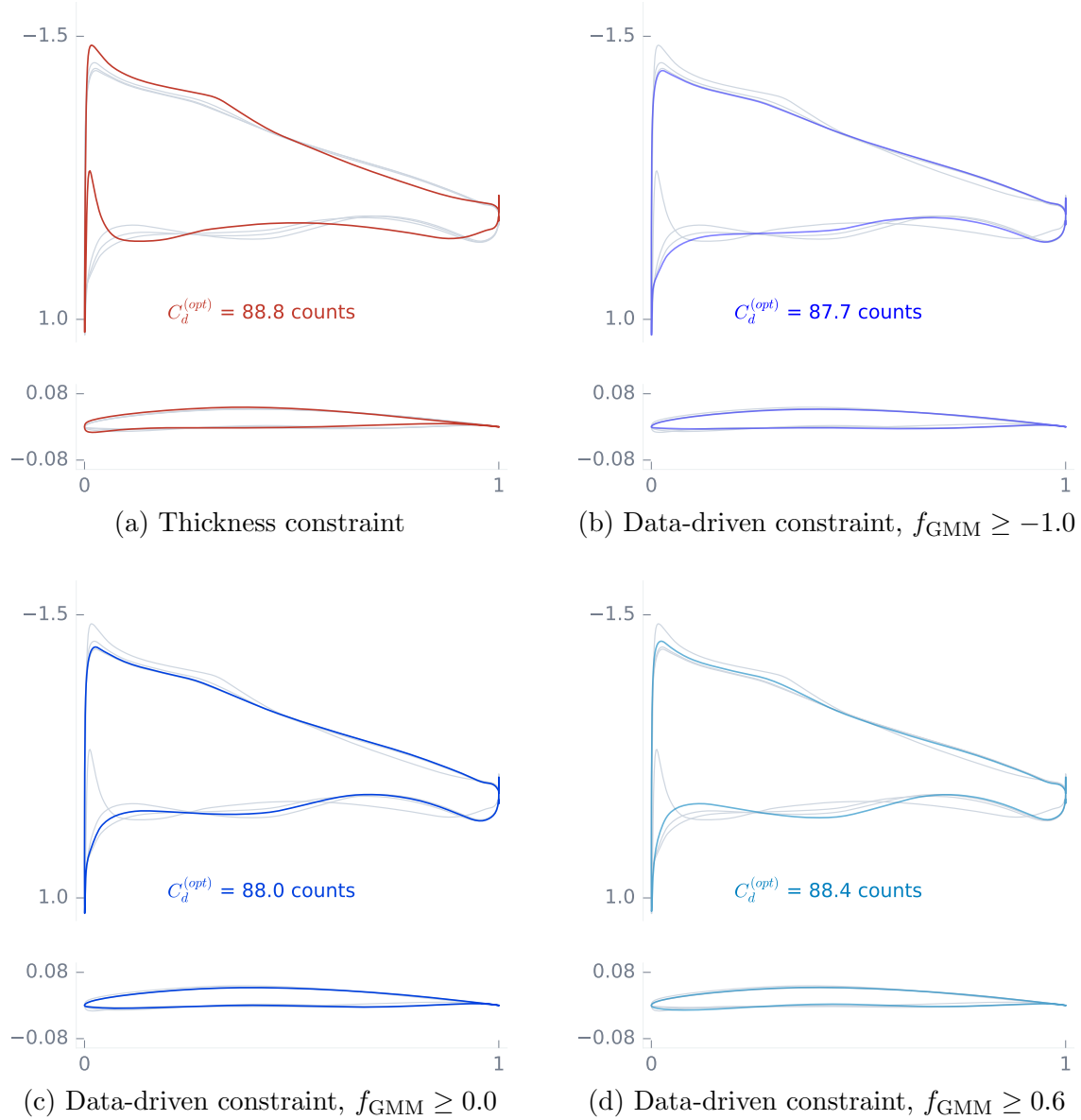


Figure 11: Optimization with different constraints.

To analyze the off-design transonic performance of the optimized airfoils, we computed the drag divergence curves and plotted them in Figure 13. The drag divergence curves for the airfoil optimized with the data-driven constraints were close to those optimized with just the basic constraint (Figure 10), while the curves of the optimized airfoil with the thickness constraint were significantly above the others. Despite the explicit constraint formulation addressing the thin leading edge issue, it sacrificed the aerodynamic performance over the whole transonic regime. The data-driven constraints, on the other hand, achieved almost the same performance as that of the basic constraint case while obtaining much more realistic airfoils.

Modifying the explicit thickness constraint according to the area constraint value may provide similar results to the data-driven constraint; however, it requires trial and

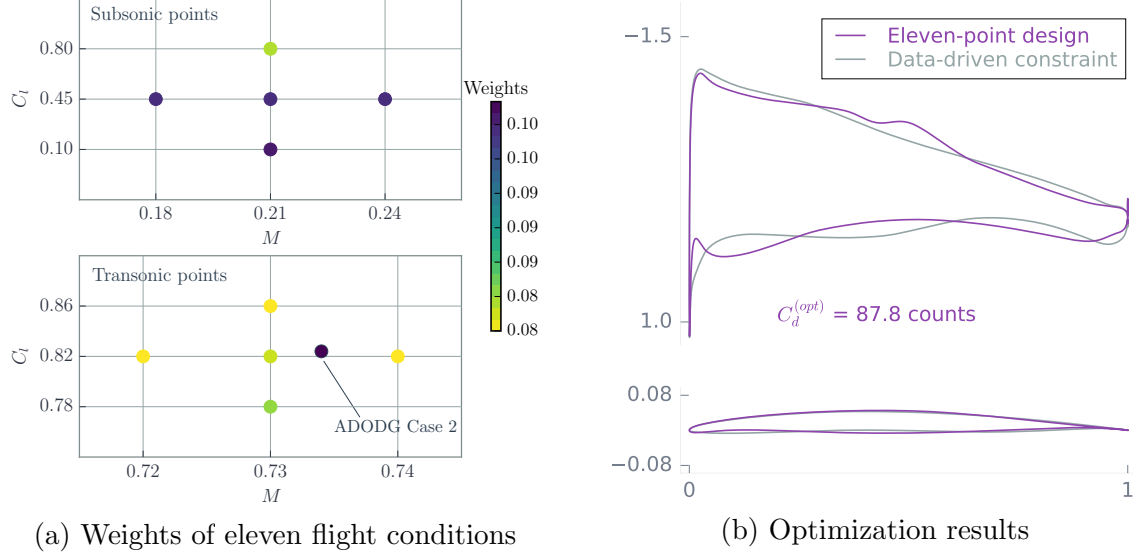


Figure 12: Eleven-point airfoil design optimization leads to a result close to the optimum from the data-driven constraint approach.

error to find the appropriate constraint value. In wing shape design optimization, this is especially difficult because the ideal sectional areas vary with the spanwise position, while the data-driven constraint is more widely applicable. Although increasing the lower bound of the data-driven constraint affects the transonic performance, the curves in Figure 13 show that the optimization still yields sensible results for different values of  $f_{GMM}$ .

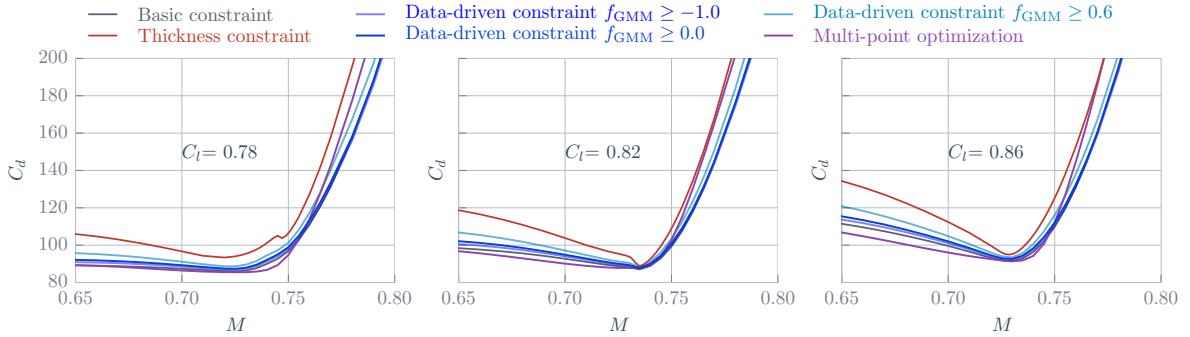


Figure 13: Optimization with the thickness constraint decreases the improvement in the transonic regime relative to the optimization with the data-driven constraint.

As shown in Figure 13, multipoint optimization achieves good performance around the cruise point; however, the drag increases severely as the speed rises, which reduces the drag-divergence Mach ( $M_{dd}$ ) numbers. Involving optimization points in the drag-divergence Mach domain could address this issue to some extent; however, we find that it makes the multipoint optimization more sensitive to the combination weights. In addition, the optimizer tends to reduce the weighted drag by decreasing the subsonic performance to increase  $M_{dd}$ , which makes the result impractical. In these circumstances,

the data-driven constraint might be a better choice than multipoint optimization.

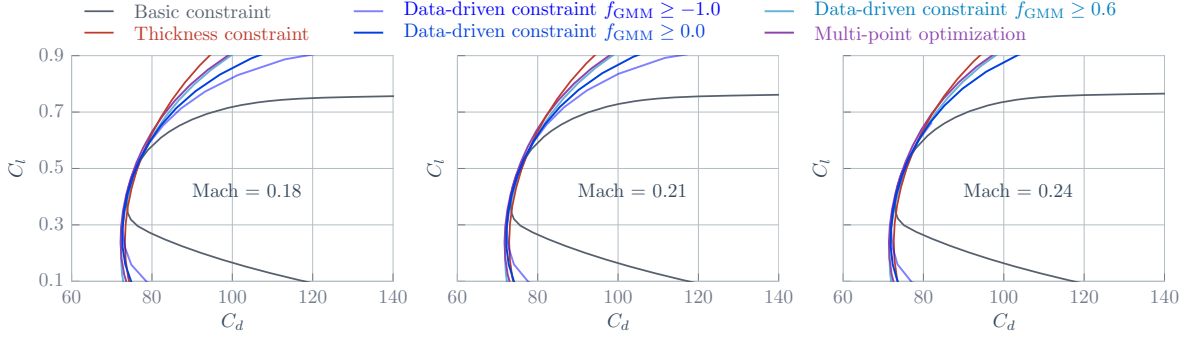


Figure 14: Improvement by the data-driven constraint to the low-speed performance of the optimized airfoil.

We also plotted the drag polars for the airfoils optimized with the data-driven constraint at different Mach numbers in the subsonic regime, as shown in Figure 14. These drag polars were much wider after adding the data-driven constraint, compared with those of the airfoil optimized with the basic constraint. Therefore, we conclude that the data-driven constraint significantly increases the low-speed performance of optimized airfoils almost without decreasing the transonic performance.

### 3.3 Impact of the Airfoil Database

Data-driven approaches rely on a wealth of data to learn the underlying patterns. The selection of an airfoil database might have an impact on the data-driven constraint and optimization results.

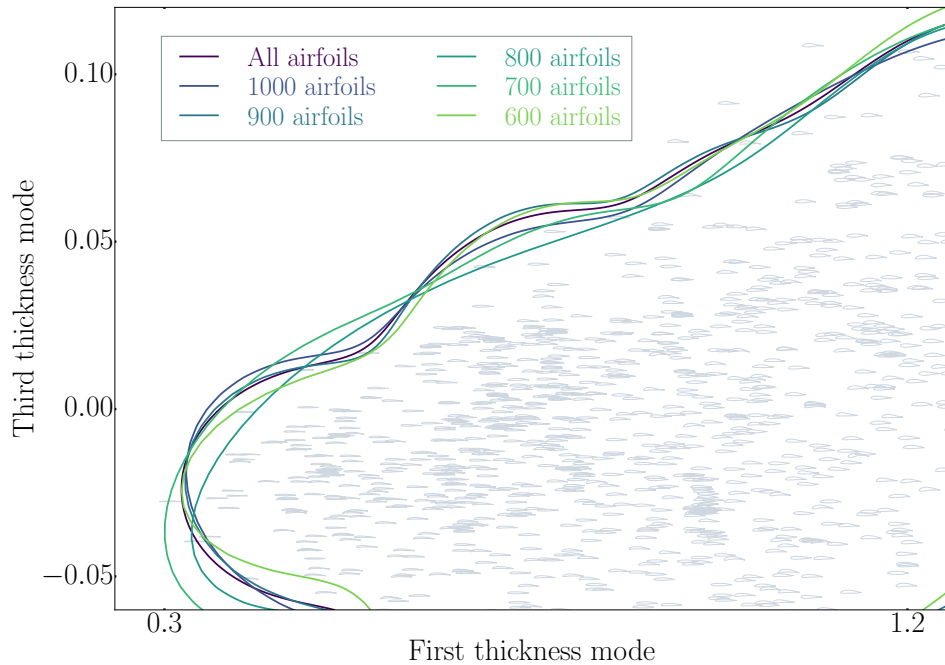


Figure 15:  $f_{GMM} = 0$  contours with GMMs trained by different airfoils.

We investigated this impact by using different airfoils in the training of the GMM. Because the airfoil database we used contains different families of airfoils and it is difficult to find another database of a similar size, we generated the training data sets by randomly selecting airfoils from this database. Owing to the transonic application of this data-driven constraint, we kept the NASA transonic airfoils in all training sets. Figure 15 shows that  $f_{\text{GMM}} = 0.0$  contours of GMMs trained by different airfoil subsets are similar. We performed airfoil optimization with  $k_{\text{aera}} = 0.4$ , using it as the data-driven constraint.

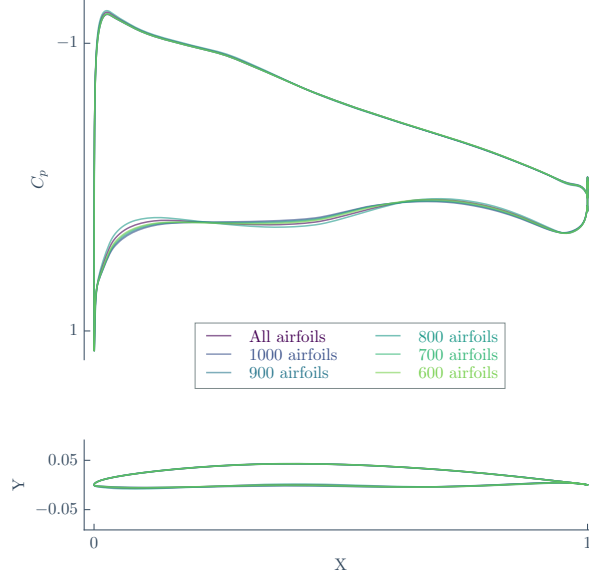


Figure 16: Optimization with data-driven constraints derived from different airfoils.

Table 2: Comparison of optimization results with data-driven constraints derived from different airfoils.

$f_{\text{GMM}}$ dataset	Optimized $\alpha$ ( $^{\circ}$ )	Optimized $C_d$ (counts)	L2 norm of difference in shapes
All airfoils	2.1333	87.66	—
1000 airfoils	2.1384	87.86	0.0069
900 airfoils	2.1358	87.80	0.0090
800 airfoils	2.1317	88.13	0.0094
700 airfoils	2.1337	87.75	0.0116
600 airfoils	2.1320	87.70	0.0145

As shown in Figure 16 and Table 2, the optimization results with GMMs trained by random subsets are all close to those optimized with the constraint derived from all airfoils, which means that different training data do not have a significant impact on the optimization with the proposed data-driven constraint.

## 4 Wing Shape Optimization

Aerodynamic shape optimization of aircraft wings is usually subject to volume or thickness constraints. A volume constraint is mainly used to ensure enough volume for the fuel. However, thickness constraints are not easy to define because they are highly dependent on the wing structure and design trade-offs between the aerodynamic and the structural performance, and it is best done directly through aerostructural optimization [37]. In a pure aerodynamic shape optimization, thickness constraints that prevent the wing shape from moving inside a reasonable baseline shape like the CRM wing will satisfy structural and manufacturing requirements. However, such strict thickness constraints sacrifice the potential improvement in aerodynamic performance [10]. Moreover, thickness constraints are even more challenging to define when a good baseline shape is not available.

Table 3: Wing optimization problem statement. This is identical to the ADODG CRM single-point wing optimization problem [10] with the addition of the proposed data-driven constraint.

	Function	Description	Quantity
Minimize	$C_D$	Drag coefficient	1
With respect to	$z_{\text{shape}}$	$z$ perturbation of the FFD control points	720
	$\alpha$	Angle of attack	1
Subject to	$C_L = 0.5$	Lift constraint	1
	$C_{M_y} \geq -0.17$	Pitching moment constraint	1
	$V \geq V_{\text{init}}$	Minimum volume constraint	1
	$t \geq 0.25t_{\text{init}}$	Minimum thickness constraints	750
	$\Delta z_{\text{TE,upper}} =$ $-\Delta z_{\text{TE,lower}}$	Fixed-wing root incidence constraint	1
	$\Delta z_{\text{LE,upper}} =$ $-\Delta z_{\text{LE,lower}}$	Fixed-wing leading edge constraints	15
	$f_{\text{GMM}}$	Data-driven constraints on sections	8

The ADODG Case 4 wing optimization benchmark <sup>5</sup> took the approach of constraining the thickness to be greater than or equal to 25% of the baseline CRM wing thicknesses at any point and the volume to be greater than or equal to the baseline [10]. This low value for the thickness constraint was chosen so as not to restrict the aerodynamic performance improvement too much. However, the optimal wings exhibited airfoil sections that were too thin to be considered practical and thin leading edges that would adversely impact low-speed performance [10, 13, 38].

We sought to address this issue in the CRM wing optimization by adding the data-driven constraints. The optimization problem statement is detailed in Table 3. This problem is identical to the ADODG CRM wing single-point optimization benchmark. The single flight condition was  $M = 0.85$  and  $Re = 5 \times 10^6$ . Following the ADODG

<sup>5</sup><http://mdolab.engin.umich.edu/content/aerodynamic-design-optimization-workshop>



benchmark case, there were 750 thickness constraints that prevented the local thickness from decreasing to less than 25% of the initial value. We used the same L2 level mesh and FFD control points used by Lyu et al. [10] (shown in Figure 17).

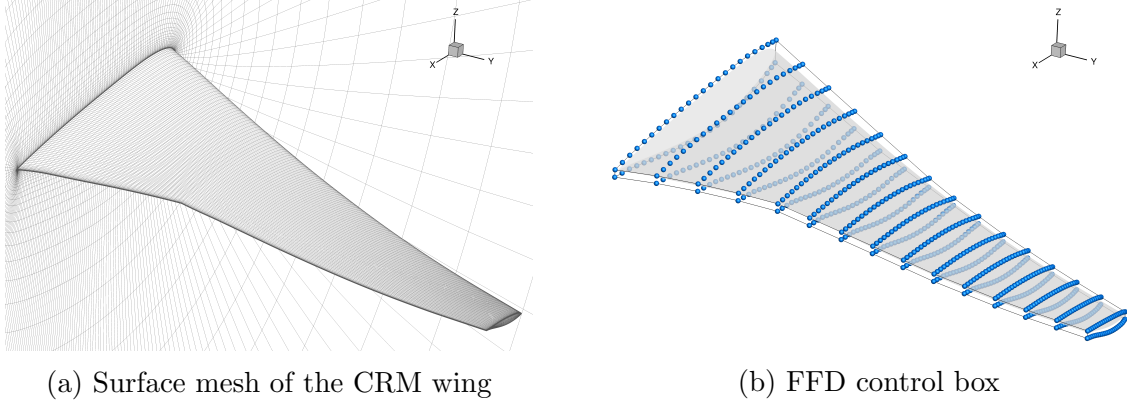


Figure 17: The mesh and FFD control box used in the CRM wing optimization

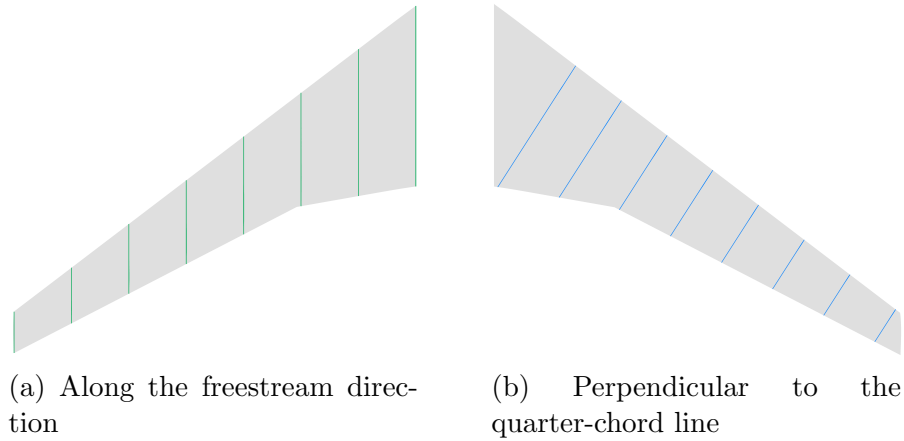


Figure 18: The two airfoil section orientations used to enforce the data-driven geometric constraints.

The data-driven constraints are intended to ensure that the  $f_{\text{GMM}}$  values for all airfoil cross sections are consistent during the optimization. We investigated two airfoil section orientations: freestream direction and perpendicular to the quarter-chord line. Both approaches enforce eight  $f_{\text{GMM}}$  constraints at airfoil sections distributed evenly from the root to the tip, as shown in Figure 18. We also solved two other optimization problems without the data-driven constraints for comparison. In total, we solved the four optimization variations on the problem detailed in Table 3:

**Basic constraints:** This problem enforces the constraints in Table 3 except for the data-driven constraints.

**Strict thickness constraints:** In addition to the basic constraints, 750 strict thickness constraints are enforced such that the optimized shape lies outside the starting shape.

**Data-driven constraints (freestream):** This solves the problem of Table 3, where the airfoils considered for the data-driven constraints are oriented in the freestream directions.

**Data-driven constraints (chord line):** Same as the above, but the airfoils in the data-driven constraints are perpendicular to the wing quarter-chord line.

## 4.1 Optimization Results With Different Constraints

Figure 19 shows the baseline CRM wing and the optimized wing subject to the basic constraints. The optimization eliminates shock waves, and, thus, the drag is significantly reduced. In addition, the optimization decreases the thickness near the leading edge, and some sections in the optimized wing, such as Sections E and F, are unrealistic.

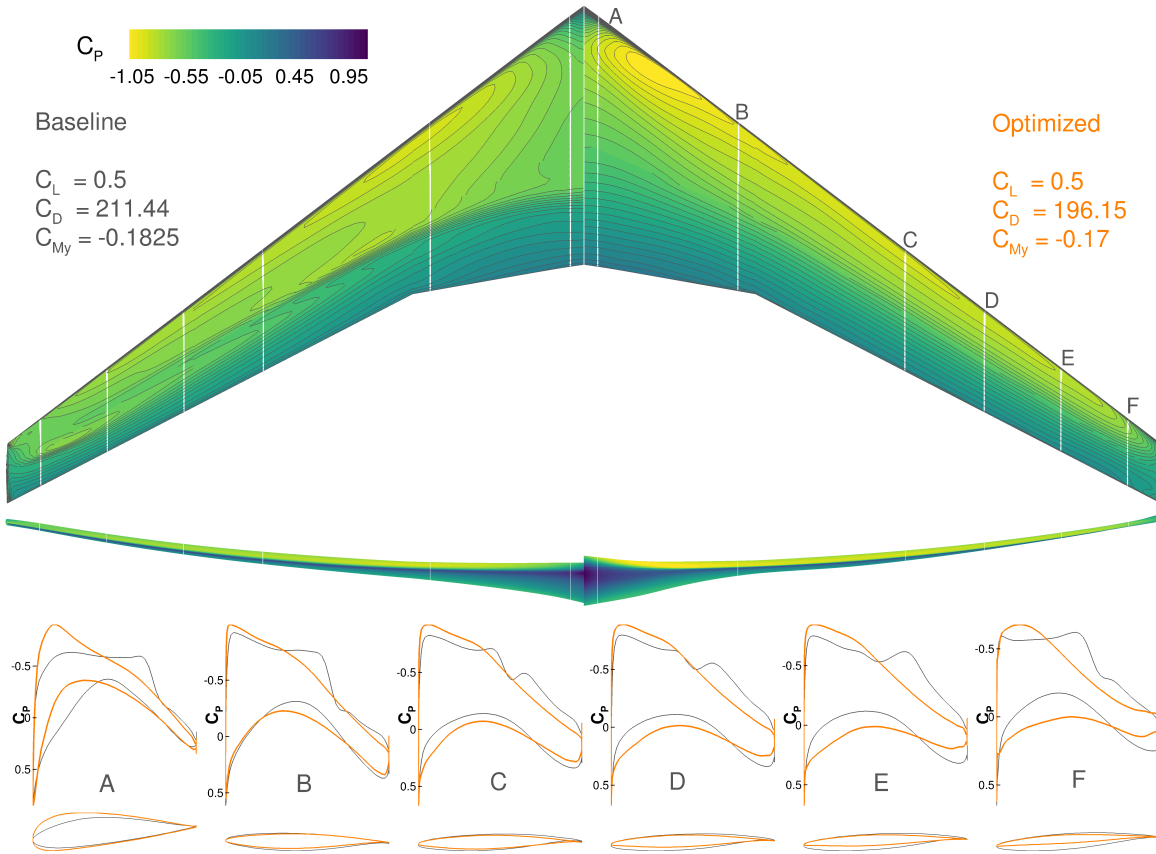


Figure 19: Optimization with the basic constraints in Table 3

Figure 20 shows that the strict thickness constraints addressed the thin leading edge issue and made the optimization converge to a reasonable shape. However, these strict thickness constraints negatively affected the optimization gains and, thus, the optimized  $C_D$  was larger than that in the optimization with the basic constraints (Figure 19) by 4.23 counts.

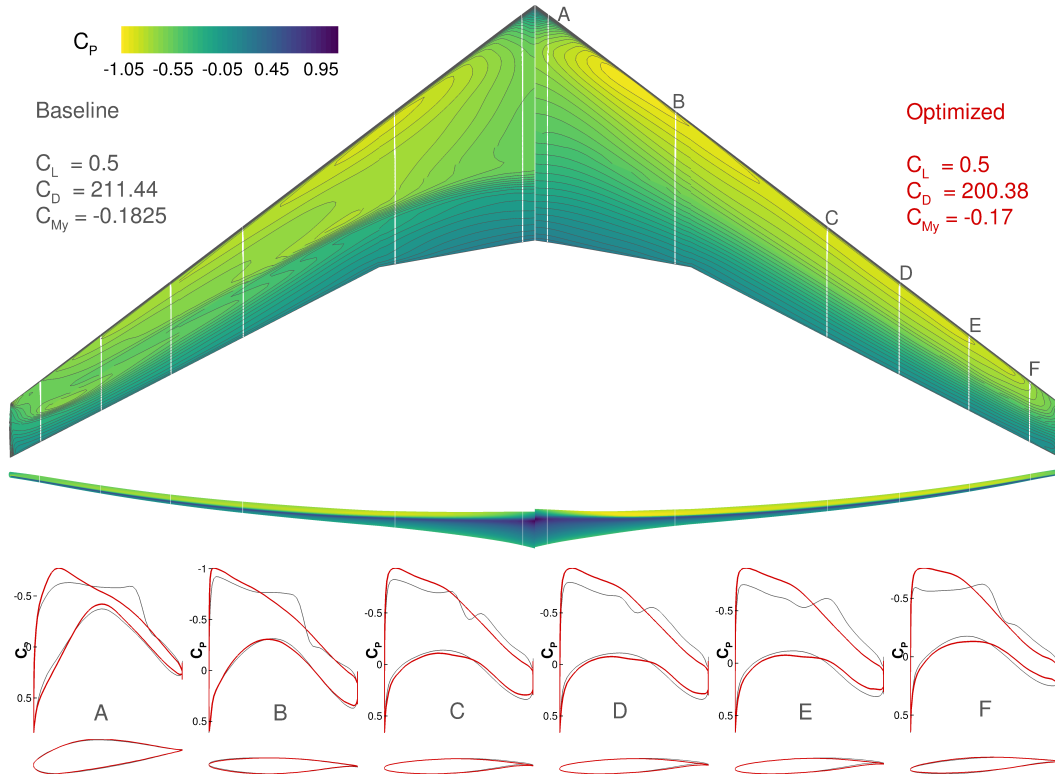


Figure 20: Optimization with the strict thickness constraints

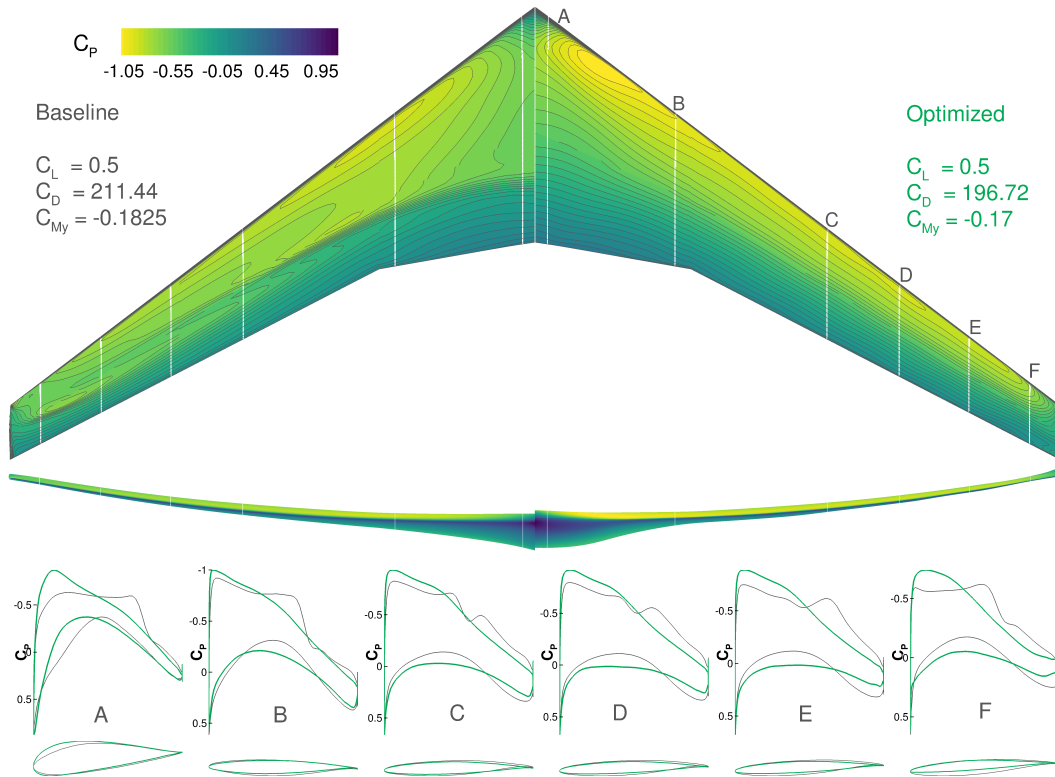


Figure 21: Optimization with data-driven constraints (free stream)

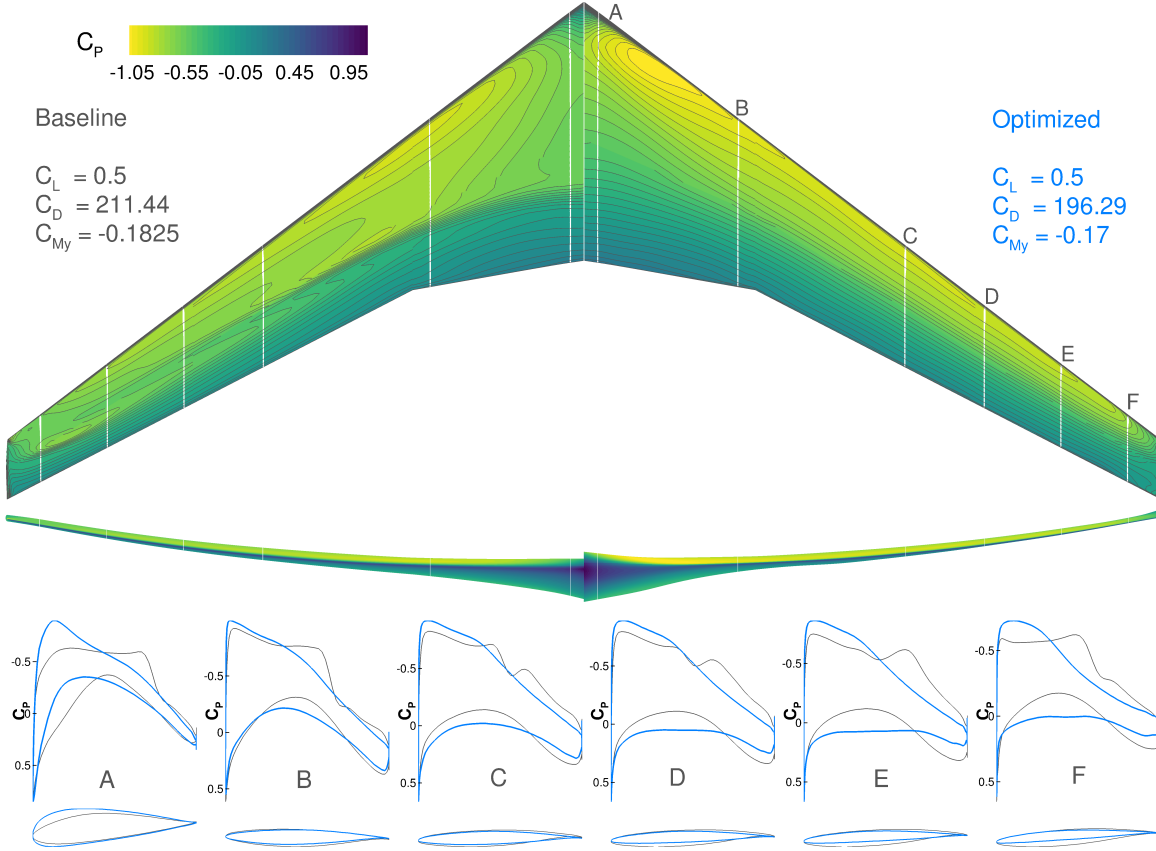


Figure 22: Optimization with data-driven constraints (chord line)

As shown in Figure 21 and Figure 22, the data-driven constraints also addressed the thin leading edge issue, and the leading edge thickness increased compared with the optimization with the basic constraints (Figure 19). More importantly, the data-driven constraint did not affect the optimization gains: the optimized drag coefficients with two different data-driven constraints were close to those achieved with the basic constraints. Applying the data-driven constraints along the freestream direction resulted in more improvements in the thin leading edge issue. The optimization results demonstrate that the data-driven constraints address the thin leading edge issue without decreasing the optimization gain in the on-design point. We discuss the aerodynamic performance of these designs by CFD evaluations in Section 4.2.

## 4.2 Aerodynamic Performance Comparison of Designs by Different Constraints

We used CFD-based RANS to compare the performance of these designs in the subsonic and transonic regimes. Figure 23 shows their drag divergence curves with different  $C_L$ , and Figure 24 shows their  $C_L$ - $C_D$  drag polars with  $M = 0.2$ .

Compared with the baseline, the optimization with the basic constraints did not have any negative effects on the off-design points when  $M > 0.84$ . That is why previous studies [10, 13] did not completely address the thin leading edge issue using a multi-

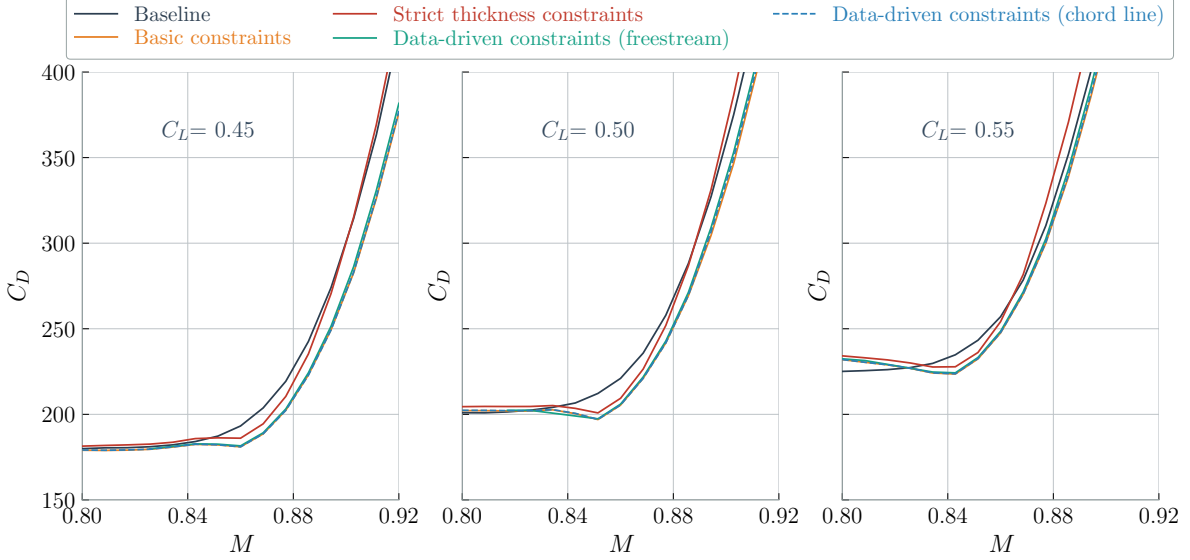


Figure 23: Drag divergence curves showing that the optimized shape with the strict thickness constraints seriously affects the optimization gains in the transonic regime.

point design in the transonic regime. The strict thickness constraints addressed the thin leading edge issue at the expense of the transonic performance. For example, in Figure 23, optimization with the strict thickness constraints only reduced the drag near the on-design point  $M = 0.85$ , while, in the regime with a larger Mach number, the drag of the optimized wing was larger than that of the baseline wing. The optimization with the strict thickness constraints did not obviously improve the performance at the on-design point but might have reduced the drag-divergence Mach number. Therefore, the strict thickness constraints are not suitable for the aerodynamic shape optimization in this case, and this type of thickness might not be suitable for other detailed aerodynamic shape optimization either.

Optimization with the data-driven constraints obviously has a better transonic aerodynamic performance. As shown in Figure 23, the curves of the data-driven constraints are similar to those of the optimization with basic constraints. In addition, enforcing the data-driven constraints on sections perpendicular to the quarter-chord line achieved a slightly better transonic performance than that of enforcing the data-driven constraints along the freestream direction. Overall, optimization with the data-driven constraints effectively reduced the drag in the transonic regime.

We also compared the subsonic performance of different designs in Figure 24, which shows the drag polar of three designs at  $M = 0.20$ . Because CFD-based RANS cannot accurately simulate flows at high angles of attack, we only provided the drag polar with  $C_L \leq 0.7$ . The design with the strict thickness constraints had a similar drag polar to that of the baseline wing, and, therefore, this constraint maintained the initial subsonic performance. The thin leading edge issue that occurred in the optimization with the basic constraints significantly affected the subsonic performance, shifted the drag polars to the right, and, thus, increased the drag overall. With the data-driven constraints, the thin leading edge issue was addressed and the drag polars shifted to

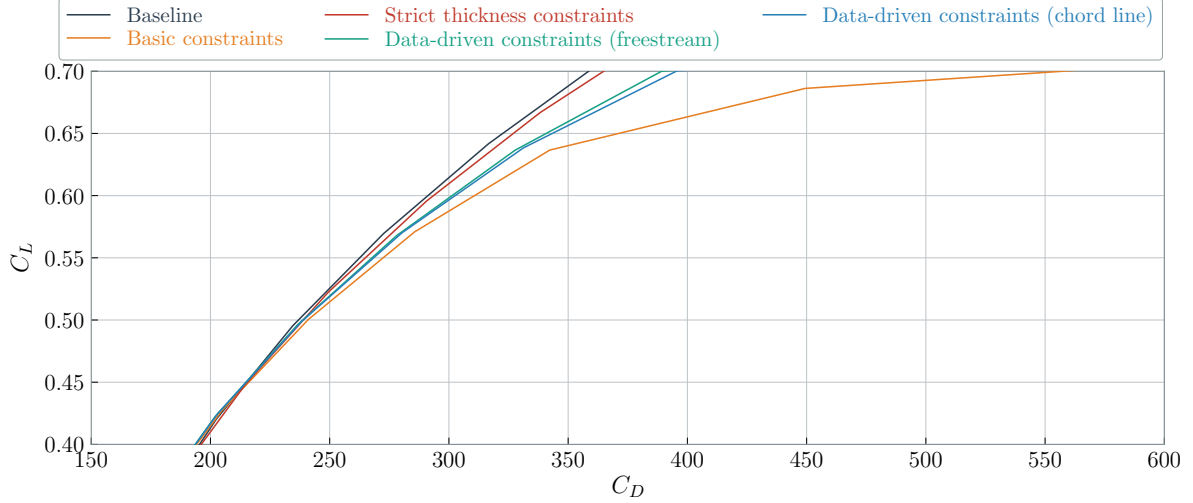


Figure 24: Improvement by the data-driven constraints to the low-speed performance of the optimized wing.

the left of the basic constraint drag polar. In addition, the data-driven constraints applied to the cross sections along the freestream direction made it more effective to improve the subsonic performance, and this was expected on the basis of the optimized shapes in Figure 21 and Figure 22.

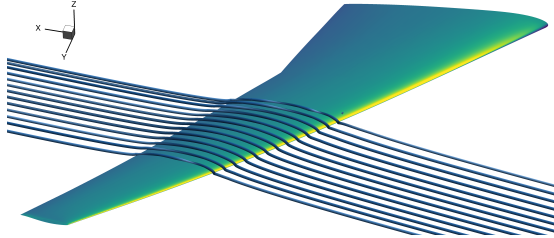


Figure 25: Flow over the baseline CRM wing with  $M = 0.2$ ,  $Re = 1.0 \times 10^6$ , and  $C_L = 0.7$

Figure 25 shows the flow over the baseline CRM wing with  $M = 0.2$ ,  $Re = 1.0 \times 10^6$ , and  $C_L = 0.7$ , and Figure 26 shows the corresponding flows over the optimized wings. The thin leading edge in the optimization with the basic constraints induced flow separations, which accounted for its larger drag. In addition, early flow separation decreased the maximum  $C_L$ , which could degrade the low-speed performance. The strict thickness constraints and the data-driven constraints delayed the separation, improving the subsonic performance of the optimized wing.

Overall, although strict thickness constraints can maintain the subsonic performance, the benefits to the on-design point are decreased. On the other hand, the data-driven constraints we developed improve the subsonic performance without losing the optimization benefits in the transonic regime. For more comprehensive wing optimization, structures should be modeled and designed concurrently [37, 39]. In addition, an accurate analysis of high-angle-of-attack flow conditions would be required.



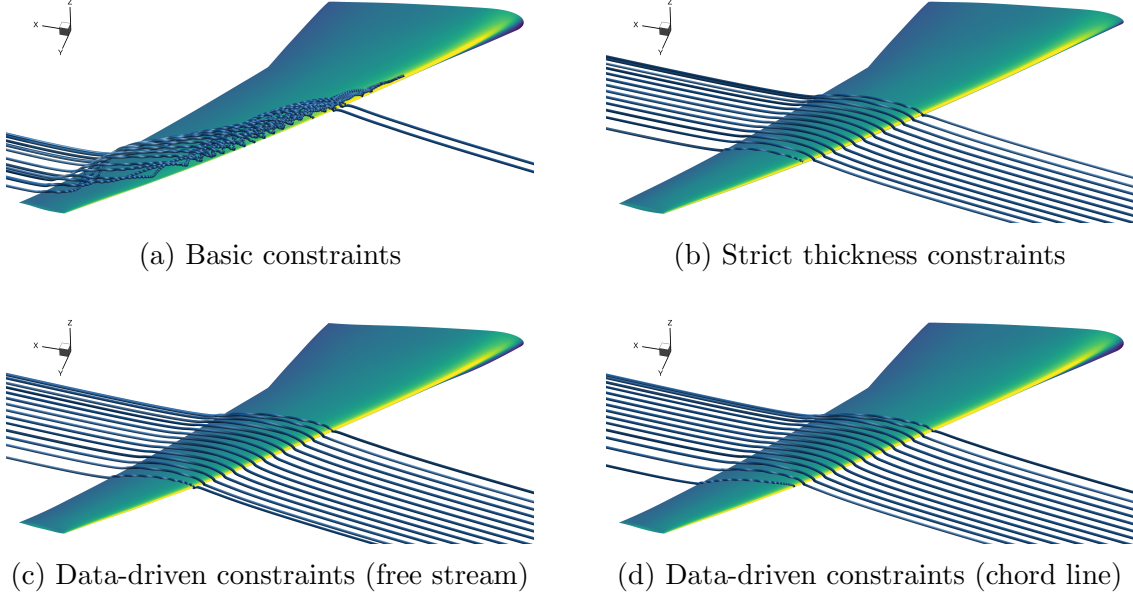


Figure 26: Flows over the wings optimized with different constraints at  $M = 0.2$ ,  $Re = 1.0 \times 10^6$ , and  $C_L = 0.7$

## 5 Conclusions

The thin leading edge issue in transonic aerodynamic shape optimization significantly affects the subsonic performance. Although the final solution to this issue is via high-fidelity multidisciplinary design optimization, it can be addressed at low computational cost by adding suitable constraints. However, explicit geometric constraints require a large amount of trial and error. We propose a data-driven approach to learn the underlying knowledge built into a database of actual airfoils. We convert the engineering experience into a continuously differentiable function through a Gaussian mixture model, which makes it viable to impose the corresponding constraint in gradient-based optimization.

Transonic aerodynamic shape optimization where the cross-sectional area is allowed to decrease is likely to sharpen the leading edge to decrease the drag, leading to thin leading edge issues, especially in the outer wing sections.

The data-driven constraint developed herein addresses this issue. Unlike the conventional approach of constraining the geometry explicitly, the data-driven constraint approach increases the off-design low-speed performance without affecting the optimization gains in the on-design transonic cruise points. Further analyses reveal that this constraint makes airfoil and wing design more robust with respect to flow conditions. Furthermore, the designs obtained with the data-driven constraints appear to be more reasonable from a structural point of view.

The proposed data-driven approach realizes the automatic conversion from design data to useful continuously differentiable constraints, which reduces manual intervention. This idea of data-driven constraints can be used in many other engineering problems where large-enough databases of actual practical designs exist.



## 6 Bibliography

### References

- [1] Jameson, A., “Aerodynamic Design via Control Theory,” *Journal of Scientific Computing*, Vol. 3, No. 3, 1988, pp. 233–260.
- [2] Skinner, S., and Zare-Behtash, H., “State-of-the-art in aerodynamic shape optimisation methods,” *Applied Soft Computing*, Vol. 62, 2018, pp. 933–962. doi:10.1016/j.asoc.2017.09.030, URL <https://doi.org/10.1016/j.asoc.2017.09.030>.
- [3] Lyu, Z., and Martins, J. R. R. A., “Aerodynamic Design Optimization Studies of a Blended-Wing-Body Aircraft,” *Journal of Aircraft*, Vol. 51, No. 5, 2014, pp. 1604–1617. doi:10.2514/1.C032491.
- [4] Buckley, H. P., Zhou, B. Y., and Zingg, D. W., “Airfoil Optimization Using Practical Aerodynamic Design Requirements,” *Journal of Aircraft*, Vol. 47, No. 5, 2010, pp. 1707–1719. doi:10.2514/1.C000256.
- [5] Li, J., Cai, J., and Qu, K., “Adjoint-Based Two-Step Optimization Method Using Proper Orthogonal Decomposition and Domain Decomposition,” *AIAA Journal*, Vol. 56, No. 3, 2018, pp. 1133–1145. doi:10.2514/1.j055773, URL <https://doi.org/10.2514/1.j055773>.
- [6] Liem, R. P., Mader, C. A., and Martins, J. R. R. A., “Surrogate Models and Mixtures of Experts in Aerodynamic Performance Prediction for Aircraft Mission Analysis,” *Aerospace Science and Technology*, Vol. 43, 2015, pp. 126–151. doi:10.1016/j.ast.2015.02.019.
- [7] Liem, R. P., Martins, J. R. R. A., and Kenway, G. K., “Expected Drag Minimization for Aerodynamic Design Optimization Based on Aircraft Operational Data,” *Aerospace Science and Technology*, Vol. 63, 2017, pp. 344–362. doi:10.1016/j.ast.2017.01.006.
- [8] Han, Z.-H., Görtz, S., and Zimmermann, R., “Improving variable-fidelity surrogate modeling via gradient-enhanced kriging and a generalized hybrid bridge function,” *Aerospace Science and Technology*, Vol. 25, No. 1, 2013, pp. 177–189. doi:10.1016/j.ast.2012.01.006.
- [9] Li, J., Cai, J., and Qu, K., “Surrogate-based aerodynamic shape optimization with the active subspace method,” *Structural and Multidisciplinary Optimization*, Vol. 59, No. 2, 2019, pp. 403–419. doi:10.1007/s00158-018-2073-5.
- [10] Lyu, Z., Kenway, G. K. W., and Martins, J. R. R. A., “Aerodynamic Shape Optimization Investigations of the Common Research Model Wing Benchmark,” *AIAA Journal*, Vol. 53, No. 4, 2015, pp. 968–985. doi:10.2514/1.J053318.

- [11] Nemec, M., Zingg, D. W., and Pulliam, T. H., “Multipoint and Multi-Objective Aerodynamic Shape Optimization,” *AIAA Journal*, Vol. 42, No. 6, 2004, pp. 1057–1065.
- [12] Puente, R., Corral, R., and Parra, J., “Comparison between aerodynamic designs obtained by human driven and automatic procedures,” *Aerospace Science and Technology*, Vol. 72, 2018, pp. 443–454.
- [13] Kenway, G. K. W., and Martins, J. R. R. A., “Multipoint Aerodynamic Shape Optimization Investigations of the Common Research Model Wing,” *AIAA Journal*, Vol. 54, No. 1, 2016, pp. 113–128. doi:[10.2514/1.J054154](https://doi.org/10.2514/1.J054154).
- [14] Kenway, G. K. W., and Martins, J. R. R. A., “Buffet Onset Constraint Formulation for Aerodynamic Shape Optimization,” *AIAA Journal*, Vol. 55, No. 6, 2017, pp. 1930–1947. doi:[10.2514/1.J055172](https://doi.org/10.2514/1.J055172).
- [15] Liem, R. P., Kenway, G. K. W., and Martins, J. R. R. A., “Multimission Aircraft Fuel Burn Minimization via Multipoint Aerostructural Optimization,” *AIAA Journal*, Vol. 53, No. 1, 2015, pp. 104–122. doi:[10.2514/1.J052940](https://doi.org/10.2514/1.J052940).
- [16] Burdette, D. A., and Martins, J. R. R. A., “Design of a Transonic Wing with an Adaptive Morphing Trailing Edge via Aerostructural Optimization,” *Aerospace Science and Technology*, Vol. 81, 2018, pp. 192–203. doi:[10.1016/j.ast.2018.08.004](https://doi.org/10.1016/j.ast.2018.08.004).
- [17] Li, J., Bouhlel, M. A., and Martins, J. R. R. A., “Data-Based Approach for Fast Airfoil Analysis and Optimization,” *AIAA Journal*, Vol. 57, No. 2, 2019, pp. 581–596. doi:[10.2514/1.j057129](https://doi.org/10.2514/1.j057129), URL <https://doi.org/10.2514/1.j057129>.
- [18] Li, J., Bouhlel, M. A., and Martins, J. R. R. A., “Data-based Approach for Fast Airfoil Analysis and Optimization,” *Journal of Aircraft*, Vol. 57, No. 2, 2019, pp. 581–596. doi:[10.2514/1.J057129](https://doi.org/10.2514/1.J057129).
- [19] Poole, D. J., Allen, C. B., and Rendall, T. C. S., “Metric-Based Mathematical Derivation of Efficient Airfoil Design Variables,” *AIAA Journal*, Vol. 53, No. 5, 2015, pp. 1349–1361. doi:[10.2514/1.j053427](https://doi.org/10.2514/1.j053427), URL <https://doi.org/10.2514/1.j053427>.
- [20] Robinson, G. M., and Keane, A. J., “Concise Orthogonal Representation of Supercritical Airfoils,” *Journal of Aircraft*, Vol. 38, No. 3, 2001, pp. 580–583. doi:[10.2514/2.2803](https://doi.org/10.2514/2.2803).
- [21] Reynolds, D., “Gaussian Mixture Models,” *Encyclopedia of Biometrics*, Springer US, 2015, pp. 827–832. doi:[10.1007/978-1-4899-7488-4\\_196](https://doi.org/10.1007/978-1-4899-7488-4_196).
- [22] Dempster, A. P., Laird, N. M., and Rubin, D. B., “Maximum likelihood from incomplete data via the EM algorithm,” *Journal of The Royal Statistical Society, Series B*, Vol. 39, No. 1, 1977, pp. 1–38.

- [23] Hartigan, J. A., and Wong, M. A., “Algorithm AS 136: A K-Means Clustering Algorithm,” *Applied Statistics*, Vol. 28, No. 1, 1979, p. 100. doi:[10.2307/2346830](https://doi.org/10.2307/2346830).
- [24] Yildirim, A., Kenway, G. K., Mader, C. A., and Martins, J. R., “A Jacobian-free approximate Newton–Krylov startup strategy for RANS simulations,” *Journal of Computational Physics*, 2019. doi:[10.1016/j.jcp.2019.06.018](https://doi.org/10.1016/j.jcp.2019.06.018), URL <https://doi.org/10.1016/j.jcp.2019.06.018>, (In press).
- [25] Mader, C. A., Martins, J. R. R. A., Alonso, J. J., and van der Weide, E., “ADjoint: An Approach for the Rapid Development of Discrete Adjoint Solvers,” *AIAA Journal*, Vol. 46, No. 4, 2008, pp. 863–873. doi:[10.2514/1.29123](https://doi.org/10.2514/1.29123).
- [26] Kenway, G. K., Mader, C. A., He, P., and Martins, J. R., “Effective adjoint approaches for computational fluid dynamics,” *Progress in Aerospace Sciences*, 2019. doi:[10.1016/j.paerosci.2019.05.002](https://doi.org/10.1016/j.paerosci.2019.05.002), URL <https://doi.org/10.1016/j.paerosci.2019.05.002>, (In press).
- [27] Kenway, G. K. W., Secco, N., Martins, J. R. R. A., Mishra, A., and Duraisamy, K., “An Efficient Parallel Overset Method for Aerodynamic Shape Optimization,” *Proceedings of the 58th AIAA/ASCE/AHS/ASC Structures, Structural Dynamics, and Materials Conference, AIAA SciTech Forum*, Grapevine, TX, 2017. doi:[10.2514/6.2017-0357](https://doi.org/10.2514/6.2017-0357).
- [28] Kenway, G. K., Kennedy, G. J., and Martins, J. R. R. A., “A CAD-Free Approach to High-Fidelity Aerostructural Optimization,” *Proceedings of the 13th AIAA/ISSMO Multidisciplinary Analysis Optimization Conference*, Fort Worth, TX, 2010. doi:[10.2514/6.2010-9231](https://doi.org/10.2514/6.2010-9231).
- [29] Gill, P. E., Murray, W., and Saunders, M. A., *User’s Guide for SNOPT Version 7: Software for Large-Scale Nonlinear Programming*, Systems Optimization Laboratory, Stanford University, California, 94305-4023, 2007. Technical Report.
- [30] Gill, P. E., Murray, W., and Saunders, M. A., “SNOPT: An SQP Algorithm for Large-Scale Constrained Optimization,” *SIAM Review*, Vol. 47, No. 1, 2005, pp. 99–131. doi:[10.1137/S0036144504446096](https://doi.org/10.1137/S0036144504446096).
- [31] Perez, R. E., Jansen, P. W., and Martins, J. R. R. A., “pyOpt: A Python-Based Object-Oriented Framework for Nonlinear Constrained Optimization,” *Structural and Multidisciplinary Optimization*, Vol. 45, No. 1, 2012, pp. 101–118. doi:[10.1007/s00158-011-0666-3](https://doi.org/10.1007/s00158-011-0666-3).
- [32] Lyu, Z., Kenway, G. K., Paige, C., and Martins, J. R. R. A., “Automatic Differentiation Adjoint of the Reynolds-Averaged Navier–Stokes Equations with a Turbulence Model,” *21st AIAA Computational Fluid Dynamics Conference*, San Diego, CA, 2013. doi:[10.2514/6.2013-2581](https://doi.org/10.2514/6.2013-2581).
- [33] Nadarajah, S., “Adjoint-Based Aerodynamic Optimization of Benchmark Problems,” *53rd AIAA Aerospace Sciences Meeting*, AIAA, 2015. doi:[10.2514/6.2015-1948](https://doi.org/10.2514/6.2015-1948).

- [34] Yang, G., and Ronch, A. D., “Aerodynamic Shape Optimisation of Benchmark Problems Using SU2,” *2018 AIAA/ASCE/AHS/ASC Structures, Structural Dynamics, and Materials Conference*, AIAA, 2018. doi:[10.2514/6.2018-0412](https://doi.org/10.2514/6.2018-0412).
- [35] He, X., Li, J., Mader, C. A., Yildirim, A., and Martins, J. R. R. A., “Robust aerodynamic shape optimization—from a circle to an airfoil,” *Aerospace Science and Technology*, Vol. 87, 2019, pp. 48–61. doi:[10.1016/j.ast.2019.01.051](https://doi.org/10.1016/j.ast.2019.01.051).
- [36] Martins, J. R. R. A., Sturdza, P., and Alonso, J. J., “The Complex-Step Derivative Approximation,” *ACM Transactions on Mathematical Software*, Vol. 29, No. 3, 2003, pp. 245–262. doi:[10.1145/838250.838251](https://doi.org/10.1145/838250.838251).
- [37] Kenway, G. K. W., and Martins, J. R. R. A., “Multipoint High-Fidelity Aerostructural Optimization of a Transport Aircraft Configuration,” *Journal of Aircraft*, Vol. 51, No. 1, 2014, pp. 144–160. doi:[10.2514/1.C032150](https://doi.org/10.2514/1.C032150).
- [38] Yu, Y., Lyu, Z., Xu, Z., and Martins, J. R. R. A., “On the Influence of Optimization Algorithm and Starting Design on Wing Aerodynamic Shape Optimization,” *Aerospace Science and Technology*, Vol. 75, 2018, pp. 183–199. doi:[10.1016/j.ast.2018.01.016](https://doi.org/10.1016/j.ast.2018.01.016).
- [39] Brooks, T. R., Kenway, G. K. W., and Martins, J. R. R. A., “Benchmark Aerostructural Models for the Study of Transonic Aircraft Wings,” *AIAA Journal*, Vol. 56, No. 7, 2018, pp. 2840–2855. doi:[10.2514/1.J056603](https://doi.org/10.2514/1.J056603).